36F.0 MICROSTRUCTURE AND PROCESSING LINKS IN BETA-TITANIUM DURING ADDITIVE MANUFACTURING

Chris Jasien (Mines)
Faculty: Amy Clarke (Mines)
Industrial Mentor: Adam Pilchak (MRL) and Lee Semiatin (AFRL)

This project initiated in Fall 2020 and is supported by the Office of Naval Research (ONR). The research performed during this project will serve as the basis for a Ph.D. thesis program for Chris Jasien.

36F.1 Project Overview and Industrial Relevance

The continued development of metal additive manufacturing (AM) over the past couple decades has expanded the applications and material classes in which these processes can be used. Titanium alloys have been at the center of this development due to their superior properties, particularly for aerospace and defense applications. Although Ti-6Al-4V has typically dominated in terms of use and research pertaining to metal AM processes, β-titanium alloys have begun to find increased use over Ti-6Al-4V (an α + β alloy), due to their increased strength-to-density ratios, among other properties [36F.1]. These β-titanium alloys differ from other classifications of titanium in that, upon quenching to room temperature from the β phase field, they may transform martensitically, or the metastable β-phase may be retained [36F.2-3].

There has been extensive investigation on the response of Ti-6Al-4V to various AM processing techniques, but there is still much to be understood when it comes to β-titanium. For this reason, this project focuses on investigating solidification and microstructure evolution of selected β-titanium alloys during AM. This includes understanding the columnar to equiaxed transition (CET) for a variety of thermal conditions, as well as thermal history effects on the microstructure. The study of β-titanium alloys will also avoid the confounding solid-state phase transformations that occur in Ti-6Al-4V during solidification. In-situ radiography experiments performed at the Advanced Photon Source (APS) at Argonne National Laboratory of simulated laser-powder bed fusion (L-PBF) of Ti-10V-2Fe-3Al (wt.%) (Ti-1023), a β-titanium alloy, allow for the determination of solid-liquid interface velocities for various solidification conditions. In conjunction with these velocities, finite element analysis (FEA) simulations, using tools such as FLOW-3D®, are also perform. These simulations provide other useful information, including predicted thermal gradients, which aid in understanding the effect of AM processing conditions on as-built microstructures. Investigation of other β-titanium alloys for L-PBF and other AM processes is also planned as part of this project.

36F.2 Previous Work

36F.2.1 SYSWELD Simulations

Using a developed Ti-1023 thermophysical property database [36F.4], raster scenarios representative of those conducted at the APS were modeled within SYSWELD. The models were calibrated through manipulation of heat source dimensions and efficiency, in order to achieve melt pool geometries consistent with those observed from the in-situ radiography experiments performed at the APS. Once calibrated, solidification velocities at the top of the melt pools predicted by the models were compared with the velocities calculated from the APS experiments. The two data sets did not completely agree, but followed the same general trends, demonstrating that SYSWELD could be used to estimate solidification trends in L-PBF melt pools.

36F.3 Recent Progress

36F.3.1 Top-Down Imaging – APS Samples

Top-down microscopy was captured for all the AM-simulated Ti-1023 specimens run at the APS. Representative spot-melts and rasters are shown below in **Figure 36F.1**. This imaging allowed for more accurate measurement of melt pool dimensions and observation of grain morphology, which aided the modeling work and development of a CET model that will be discussed in the following sections.

36F.3.2 CET Modeling of Ti-1023

An important tool for predicting as solidified grain morphology in AM is the use of alloy-specific solidification maps. The combination of thermal gradients and velocity during solidification allows for prediction of whether a fully columnar, fully equiaxed, or mixed microstructure is obtained. From this information, process parameters can be tailored in order to favor formation of one specific grain morphology over another. Ti-6Al-4V is the only titanium alloy that currently has a widely accepted solidification map [36F.5]. While this provides useful approximations for the solidification conditions at which the CET occurs in titanium alloys, a more exact model for Ti-1023 is desired. A prediction of the CET for Ti-1023 was developed using the Kurz-Giovanola-Trivedi (KGT) model [36F.6]. *Thermo-Calc* software was utilized to calculate the equilibrium solute liquidus slopes and partition coefficients for vanadium, iron, and aluminum, while other KGT-model inputs were obtained from literature. The exact model parameters used in this CET model are presented below in **Table 36F.1**. Using all of these inputs, a solidification map for Ti-1023 is predicted (**Figure 36F.2**).

36F.3.3 FLOW-3D® Simulations

Conduction-only programs like *SYSWELD* do not take into account fluid dynamics, which more accurately capture the intricacies of L-PBF processing. For this reason, FLOW-3D®, a computational fluid dynamics tool, was utilized to simulate the APS experiments. To correctly model each scenario, it was first necessary to classify whether the experiment exhibited a conduction or keyholing mode, as schematically shown in **Figure 36F.3**. Conduction mode is characteristic of low laser powers, where a wide and shallow pool is created due to much of the laser being reflected off the surface of the substrate. Higher powers typically result in keyholing mode, which is a more complex scenario, where a deep and narrow melt pool is created with evaporation of weld metal occurring within the melt. This important distinction determines which conditions need to be activated within the model. To classify our 82W, 139W, and 197W spot-melt experiments, the in-situ radiography for each condition was observed to determine the mode present for each power. The 82W scenario was determined to be in conduction mode, while the 139W and 197W were in keyholing modes. Using this information, simulations were run using thermophysical properties shown below in **Table 36F.2**. Predicted melt pool geometries were compared to measurements from both the in-situ radiography and post-mortem microscopy (**Table 36F.3**). Once the spot melt scenarios were completed, a similar procedure was utilized to model three raster experiments. Process parameters and observed mode for each raster are listed in **Table 36F.4**. Steady-state lengths and depths observed in the in-situ radiography experiments of the rasters were used to calibrate the models. With all spot-melt and raster models completed, predicted solidification conditions for each situation were obtained and compared to experimental values. **Figure 36F.4a&b** show example plots of solidification velocity comparisons for a spot-melt and raster, respectively. The predictions do not exactly match the experimental data, however the values and trends are similar. For the spot-melt, solidification begins slowly and increases until the melt pool is fully solidified. The raster solidification velocity increases until it reaches steady state and remains relatively constant until the laser is shut off. Solidification velocities obtained experimentally were limited in capture frequency, which may explain the inability to record the sharp increase in velocity during the final stages of solidification. **Figure 36F.5a** shows a spot melt's predicted thermal gradients and solidification velocities overlaid on the previously presented Ti-1023 solidification map. The predicted grain morphologies at various locations were compared to those observed from top-down, post-mortem microscopy. In **Figure 36F.5b**, a fully columnar structure is observed at the edge of the spot-melt, which is predicted by the combination of thermal gradient and solidification velocity (**Figure 36F.5a**). During the final stages of solidification, the spot-melt transitions from fully columnar to a mixed (**Figure 36F.5c**). Again, the solidification conditions at this location in the spot-melt correspond to those predicted by the solidification map. The same investigation was completed for the solidification conditions of a raster and is presented in **Figure 36F.6a-c**. Initial solidification of the raster is predicted to possess a fully columnar grain morphology, similar to the spot-melt discussed above (**Figure 36F.6b**). When the laser turns off and the final material solidifies, the solidification conditions predict a mixed microstructure (**Figure 36F.6c**). The equiaxed region is more defined than that observed in the spot-melt, even though solidification conditions for the raster are closer to the fully columnar region. This is likely due to the fact that solidification maps are only predictions of grain morphologies, but more investigation is needed to further calibrate this Ti-1023 map to better reflect the processing conditions. Electron backscatter diffraction (EBSD) of the sample cross sections will provide more information on the grain morphology throughout the whole melt pool, rather than just the top surface.

36F.3.4 Sigmajig Crack Susceptibility Testing

A new capability has been established at Mines to access the cracking behavior of metal alloys under AM-like conditions using the Sigmajig test, a weldability test originally developed by Goodwin [36F.11]. The Sigmajig test subjects a sample to a tensile load while an autogenous weld is created along the centerline (**Figure 36F.7**). After this processing, the sample is inspected and any cracking is quantified. For the purposes of our testing, the weld is replaced with an autogenous raster using a laser. In order to modify this test for L-PBF, a chamber that could house the Sigmajig and tightly control the atmosphere was needed. The chamber also needed to be compatible with a L-PBF test-bed housed in the Physics department. After considering all of these factors, a chamber was designed, fabricated, and assembled. A labeled diagram of the test setup is provided in **Figure 36F.8**.

36F.4   Plans for Next Reporting Period

- Continue performing *FLOW-3D* simulations for overlapping raster and spot melt scenarios;
- Continue Sigmajig crack susceptibility testing on Ti-5553;
- Cross-section EBSD of spot-melt and raster APS samples;
- Further refine Ti-1023 CET model.

36F.5   References

[36F.1] Duerig, T.W., Terlinde, G.T., Williams, J.C., 1988. Phase Transformations and Tensile Properties of Ti-10V-2Fe-3Al. Metallurgical Transactions A, 11A, 579–583.

[36F.2] Duerig, T.W., Williams, J.C., 1984. Beta Titanium Alloys in the 80s: Proceedings of the Symposium. Metallurgical Society of AIME, 19–67.

[36F.3] Lutjering, G., Williams, J.C., 2007. Alloy Classification, in: Derby, B. (Ed.), Titanium, Springer, Berlin, 33-36.

[36F.4] Jasien, C., Clarke, A.J., Microstructure and Processing Links in Beta-Titanium during Additive Manufacturing, CANFSA Report, Project 36F, April 6, 2021.

[36F.5] Kobryn, P.A., Semiatin, S.L., 2003. Microstructure and texture evolution during solidification processing of Ti–6Al–4V. J. Mater. Process. Technol., 135, 330-339.

[36F.6] Kurz, W., Giovanola, B., Trivedi, R., 1986. Theory of Microstructural Development during Rapid Solidification. Acta Metall., 34, 823-830.

[36F.7] Liu, D., Wang, Y., 2019. Mesoscale multi-physics simulation of rapid solidification of Ti-6Al-4V alloy. Additive Manufacturing, 25, 551-562.

[36F.8] Rolchigo, M.R., LeSar, R., 2018. Modeling of binary alloy solidification under conditions representative of Additive Manufacturing. Computational Materials Science, 150, 535-545.

[36F.9] Bayat, M., et al., 2019. Keyhole-induced porosities in Laser-based Powder Bed Fusion (L-PBF) of Ti6Al4V: High-fidelity modelling and experimental validation. Additive Manufacturing, 30, 1-18.

[36F.10] FLOW-3D Users Site. Melting Tutorial.

[36F.11] Goodwin, G.M., 1987. Development of a New Hot-Cracking Test – The Sigmajig, Welding Research Supplement, 33-38.
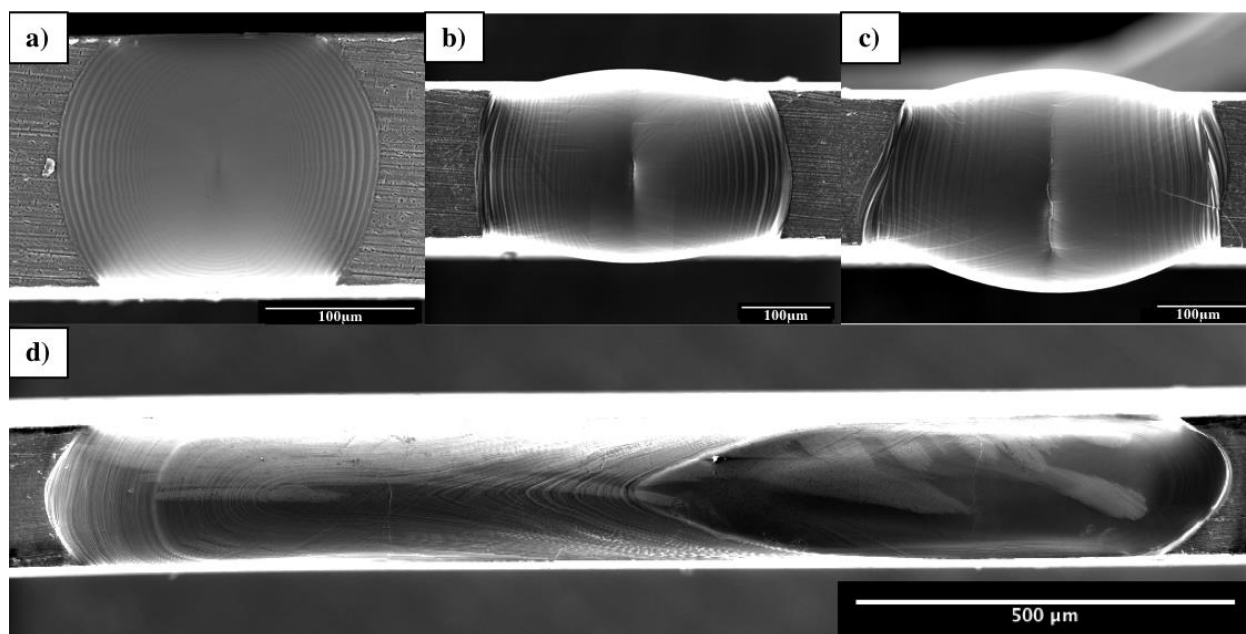
36F.6   Figures and Tables

Figure 36F.1: Top-down SEI of **a)** 82W spot-melt **b)** 139W spot-melt **c)** 197W spot-melt **d)** 139W and 0.5m/s raster.

Table 36F.1: CET parameters used in KGT model

Quantity		Value
Solute Diffusivity [36F.7]		7.9e-9 m/s^2
Gibbs-Thomson coefficient [36F.8]		5e-7 m·K
Nucleation Undercooling		5 K
Nuclei Density		1e15 nuclei/m^3
Equilibrium liquidus slope	Vanadium	0.756 K/wt.%
	Iron	0.317 K/wt.%
	Aluminum	0.894 K/wt.%
Equilibrium solute partition coefficient	Vanadium	-4.744
	Iron	-12.841
	Aluminum	-5.932

36F.4
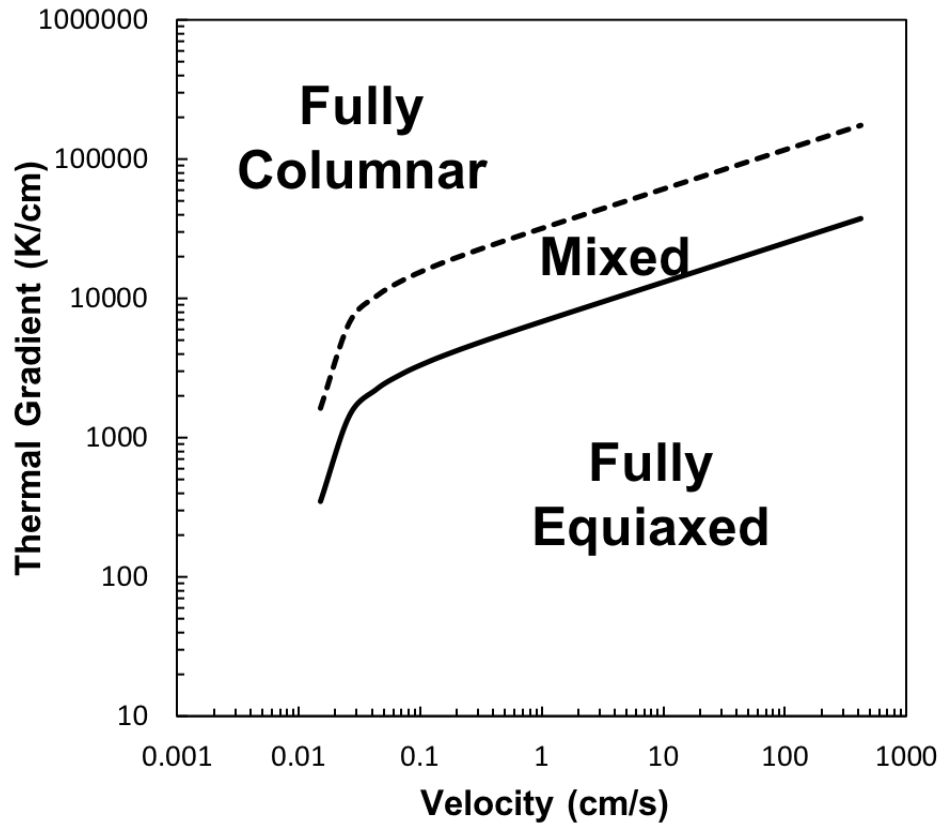
Figure 36F.2: Developed solidification map of Ti-1023 alloy using KGT model and parameters from Table 36F.1.
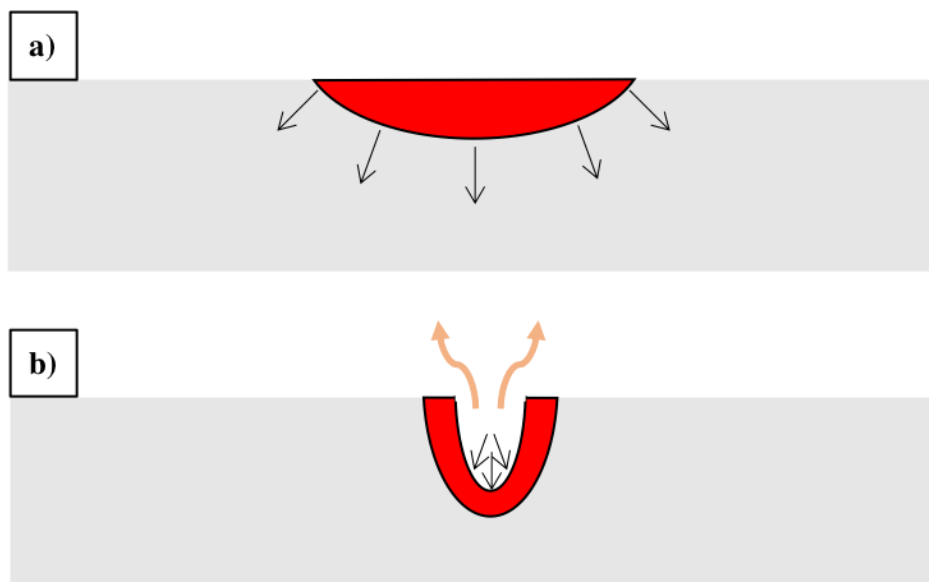

Figure 36F.3: Schematic of two laser modes showing difference in heat flow and resulting melt pool geometry for **a)** conduction and **b)** keyholing.
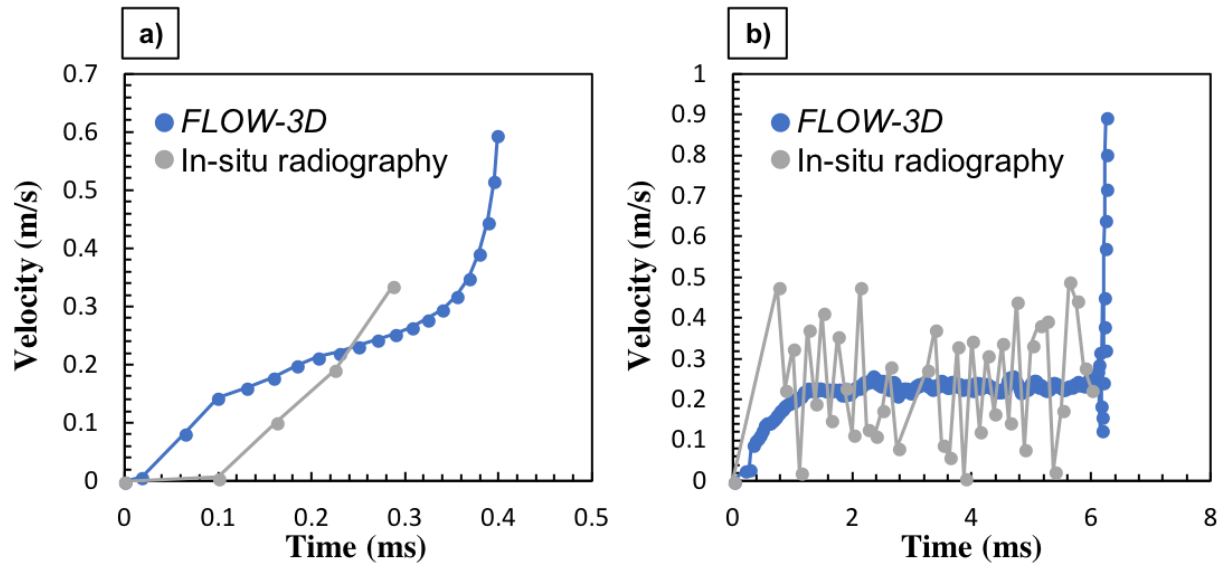
36F.5

Figure 36F.4: Plots of solidification velocity as a function of time using predicted values from *FLOW-3D* and experimentally obtained for **a)** a spot melt and **b)** raster. Note: the starting time in a) is when the laser is turned off.

Table 36F.2: Thermophysical properties used for Ti-1023 FLOW-3D simulations

Property	Value	Source
Surface Tension Coefficient	1.5 N/m	[36F.9]
Surface Tension Temperature dependence	-0.00026 N/m/K	[36F.9]
Liquidus Temperature	1883 K	[36F.4]
Solidus Temperature	1798 K	[36F.4]
Vaporization Temperature	3315 K	[36F.9]
Latent Heat of Vaporization	9.7 MJ/K	[36F.9]
Accommodation Coefficient	0.54	[36F.9]
Vapor Specific Heat	1.25e7 $cm^2/s^2/K$	[36F.10]
Fresnel Constant	0.25	[36F.10]

Table 36F.3: Comparison of experimental and model predicted melt pool geometries
Note: 139W and 197W conditions are can still be better calibrated

Power (W)	Dimension	Experiment (µm)	Model (µm)	Percent Error (%)
82	Width	220	224	1.8
	Depth	75	72	4.3
139	Width	350	373	6.6
	Depth	200	229	14.5
197	Width	390	323	17.2
	Depth	310	257	17.1

Table 36F.4: Process parameters and observed mode for modeled rasters

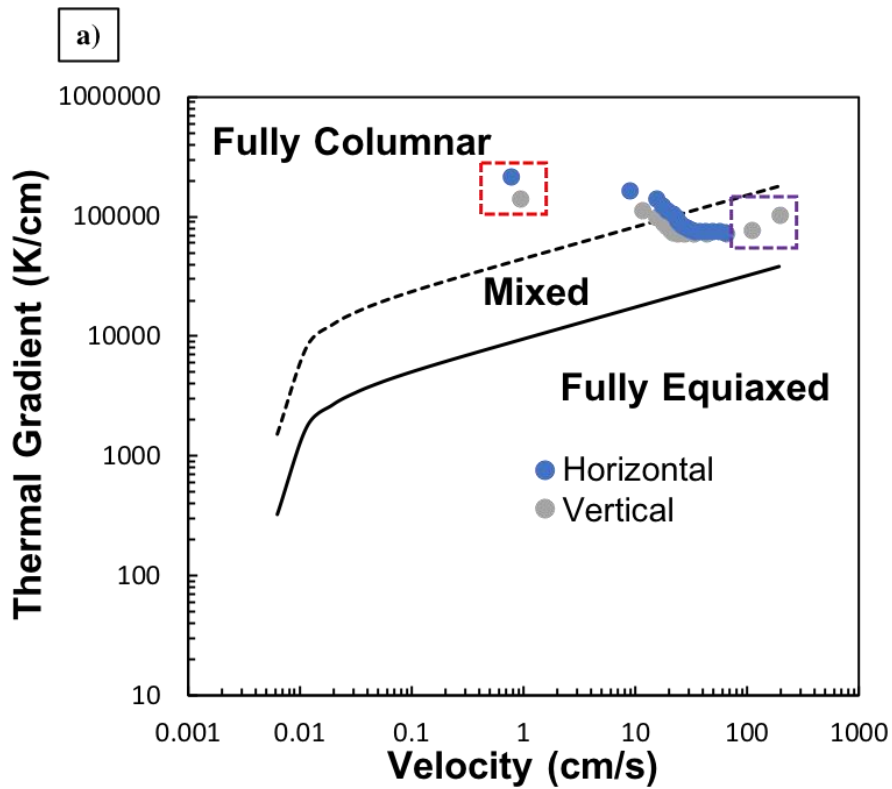| Power (W)	Travel Speed (m/s)	Mode
53.5	0.25	Conduction
82	0.5	Conduction
139	0.5	Keyholing
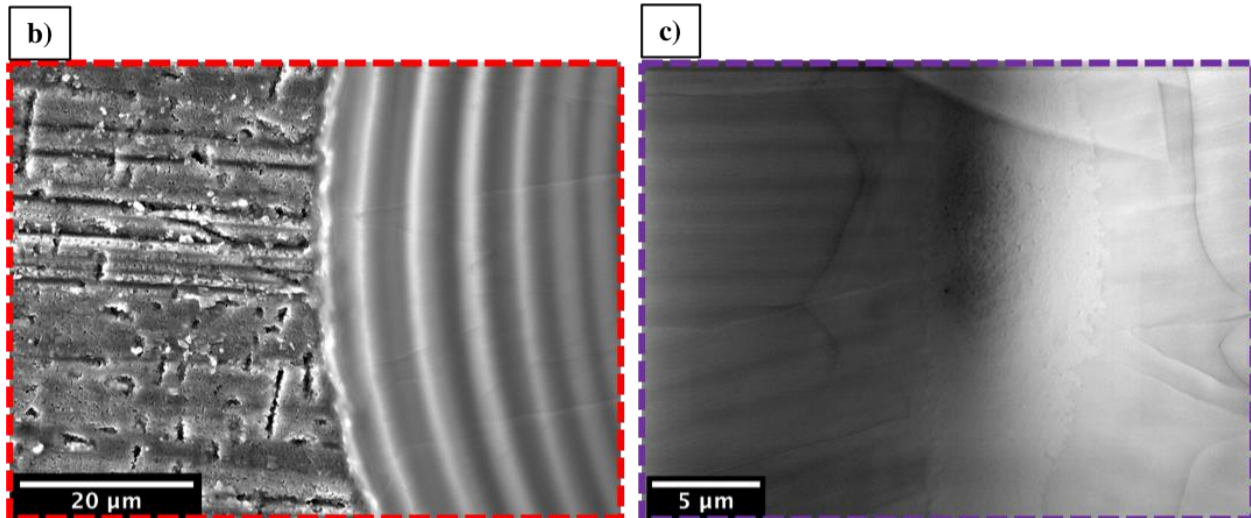
Figure 36F.5: **a)** Thermal gradient and velocity solidification conditions for 82W spot-melt overlaid on the solidification map in Figure 36F.2 **b)** top-down SEI of the melt pool edge **c)** top-down SEI of the melt pool center. Note: colored boxes in a) correlate to the approximate locations shown in b) and c).
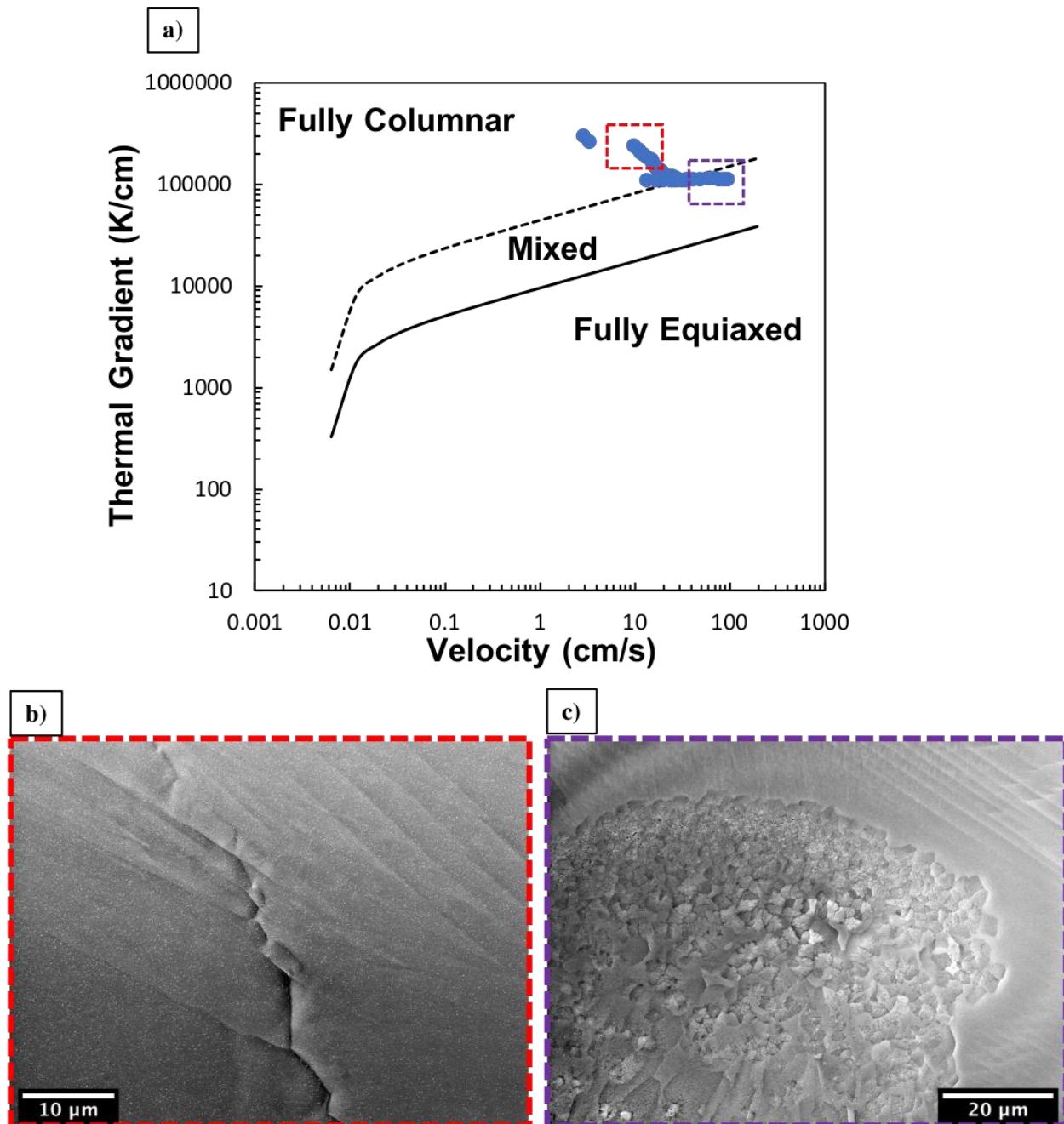
36F.8

Figure 36F.6: **a)** Thermal gradient and velocity solidification conditions for 53.5W and 0.25m/s raster overlaid on the solidification map in Figure 36F.2 **b)** top-down SEI at the beginning of the raster **c)** top-down SEI at the end of the raster. Note: colored boxes in a) correlate to the approximate locations shown in b) and c).
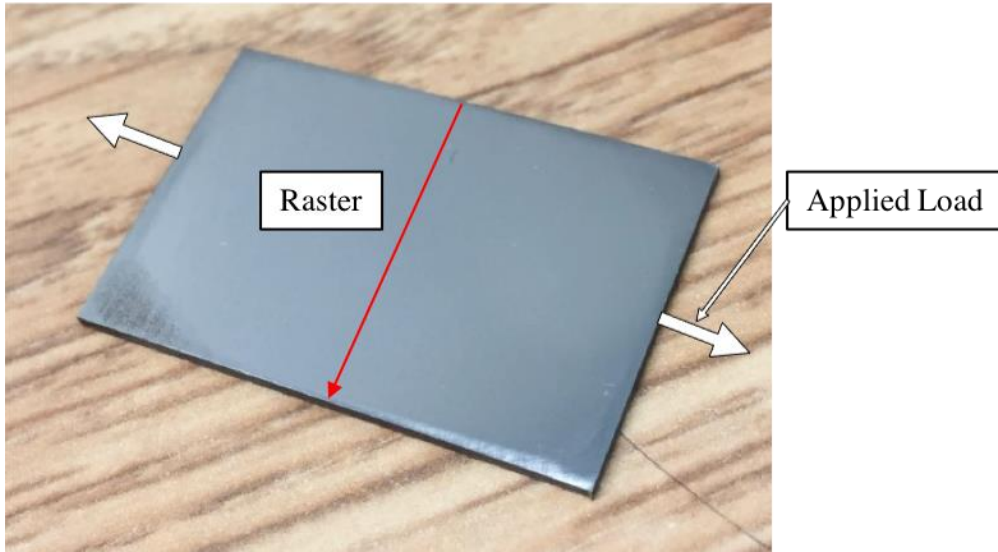
Figure 36F.7: Picture of a general test specimen labeled with direction of applied load and approximate raster location.
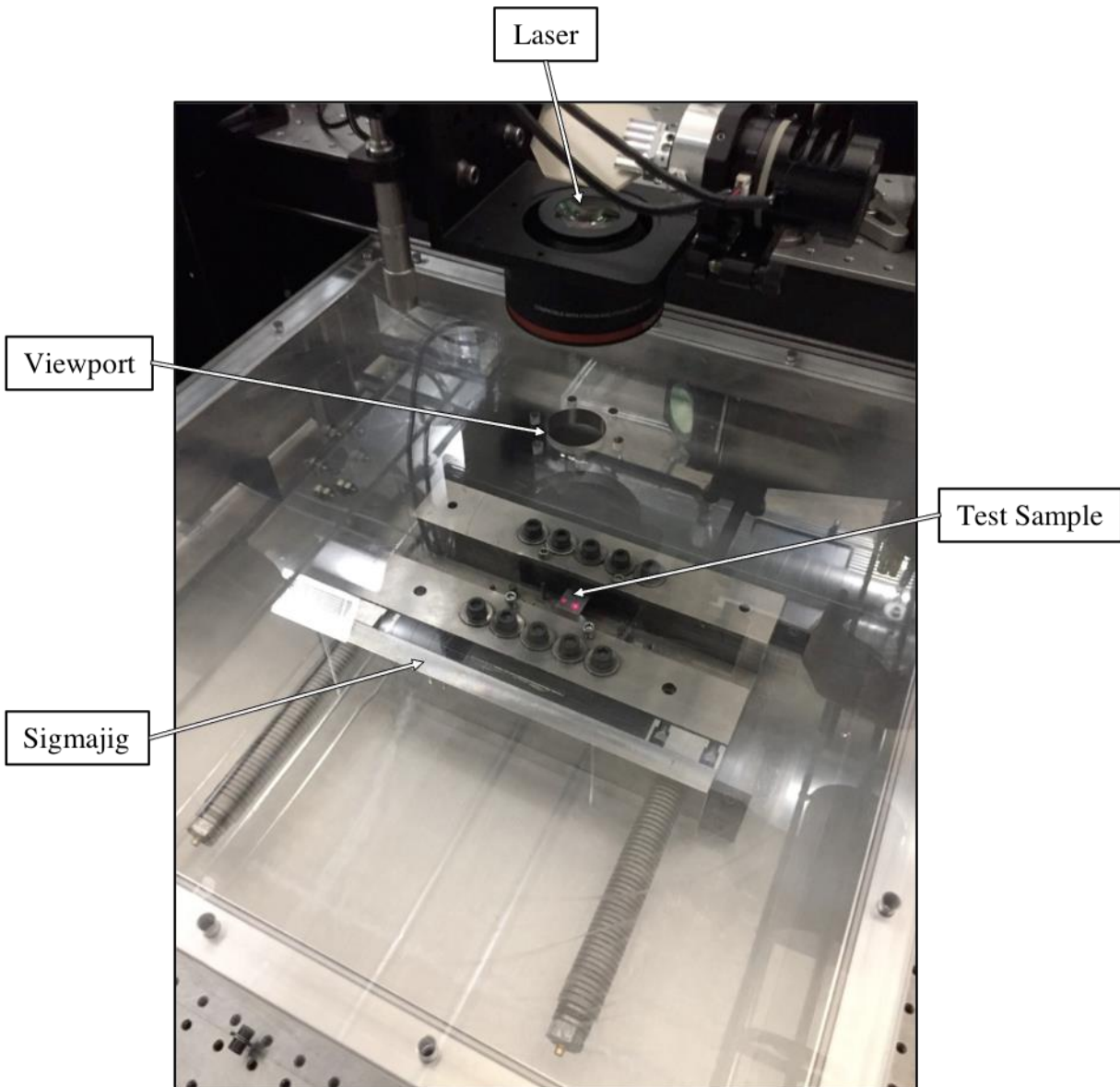
Figure 36F.8: Labeled diagram of the Sigmajig crack susceptibility experimental setup.